Evolution of interorbital superconductor to intraorbital spin-density wave in layered ruthenates

Austin W. Lindquist,[1] Jonathan Clepkens,[1] and Hae-Young Kee[1,2,*]

[1]*Department of Physics and Center for Quantum Materials, University of Toronto, 60 St. George Street, Toronto, Ontario M5S 1A7, Canada*

[2]*Canadian Institute for Advanced Research, Toronto, Ontario M5G 1Z8, Canada*

(Received 25 November 2021; revised 8 March 2022; accepted 18 April 2022; published 9 May 2022)

The ruthenate family of layered perovskites has been a topic of intense interest, with much work dedicated to the superconducting state of Sr_2RuO_4. Another long-standing puzzle is the lack of superconductivity in its sister compound, $Sr_3Ru_2O_7$, which constrains the possible mechanisms of Sr_2RuO_4. Here we address a microscopic mechanism that unifies the orders in these materials. Beginning from a model of Sr_2RuO_4 featuring interorbital spin-triplet pairing via Hund's and spin-orbit couplings, we find that bilayer coupling alone enhances, while staggered rotations destroy interorbital superconductivity. A magnetic field then shifts van Hove singularities, allowing intraorbital spin-density wave order to form in $Sr_3Ru_2O_7$. Our theory predicts that $Sr_3Ru_2O_7$ without staggered rotations exhibits interorbital superconductivity with a possibly higher transition temperature.

DOI: 10.1103/PhysRevResearch.4.023109

I. INTRODUCTION

Multiorbital systems in which the low-energy behavior is affected by various orbitals provide an ideal setup for the formation of rich electronic phases. One notable example is the family of layered perovskites, $Sr_{n+1}Ru_nO_{3n+1}$. Much attention has been paid to the single-layer material, Sr_2RuO_4 (214), which displays superconductivity (SC) at low temperatures [1–4]. However, despite intense studies, the nature of the superconducting state still remains a topic of debate [4,5]. Interest in the bilayer material, $Sr_3Ru_2O_7$ (327), grew after significant anisotropy in the resistivity, signaling an electronic nematic phase, was reported [6–12]. More recently, a resistivity linear in temperature [13] as well as spin-density wave (SDW) order were found to occur at low temperatures at field values coinciding with the presumed nematic phase, bounded by metamagnetic transitions [14–17].

A long-standing puzzle in this family is the lack of SC in 327, constraining the possible superconducting mechanisms of 214. The similarity of these materials means that a model of 214 should be able to explain the lack of SC in 327 and the sensitivity to the differences between the two. The two notable differences introduced by the second layer in 327 are the bilayer coupling and the staggered rotations of the oxygen octahedra. The observation of SDW order in the presence of a magnetic field in 327 suggests a delicate competition between SC and SDW in these two sister compounds, calling for a unified picture.

Here, we address the microscopic mechanism of the evolution from SC in 214 to SDW in 327. We show that the absence of SC in 327 supports interorbital pairing in 214 which is sensitive to orbital mixing via spin-orbit coupling (SOC). Using the same parameter set for the Kanamori Hamiltonian, we find interorbital spin-triplet SC is destroyed by the staggered rotations of the octahedra, and intraorbital SDW order emerges under a magnetic field in 327. Further, we predict that ideal bilayer 327 without staggered rotations of the octahedra, denoted $(327)_0$, displays interorbital SC with a transition temperature possibly higher than 214, as shown in Fig. 1, the phase diagram of these systems in a field.

II. MICROSCOPIC THEORY

Sr_2RuO_4 was once thought to be a leading candidate for $p+ip$ spin-triplet SC [18,19]. However, recent NMR data showing a drop in the Knight shift below the superconducting transition temperature seems to rule out odd-parity spin-triplet pairing [20,21]. While p-wave states may not explain the Knight shift reduction, spin-triplet proposals remain possible with even-parity interorbital spin-triplet states [22–29]. This pairing in the orbital basis is spin-triplet, but appears as pseudospin-singlet in the band basis due to SOC. The interorbital nature of the pairing means that significant band degeneracy near the Fermi level is required [30,31]. Alternatively, when SOC and band separation are comparable in energy, SOC stabilizes interorbital pairing via mixing of orbitals and spin [22,26,28,29,32–36].

We adopt the Kanamori Hamiltonian, well known for multiorbital systems, to investigate competition between SC and SDW order in 214, $(327)_0$, and 327. In multiorbital systems, the distinction between intraorbital, interorbital-singlet, and interorbital-triplet pairings must all be considered. Among all possible order parameters, inter- and intraorbital SDW and interorbital SC occur via attractive interactions; however, interorbital SDW is small compared to intraorbital SDW and

*hykee@physics.utoronto.ca

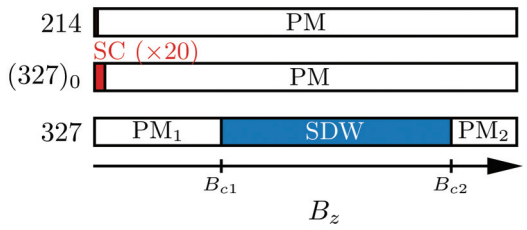

FIG. 1. Phase diagram of the single-layer, 214, ideal bilayer (no staggered rotations), $(327)_0$, and real bilayer, 327. 214 features superconductivity at small fields, expanded in $(327)_0$. Both regions are expanded by a factor of 20 to more clearly show their relative sizes. In 327, SC is destroyed by rotations of the octahedra, and SDW order exists at finite-field values between B_{c1} and B_{c2}. The values of B_{c1} and B_{c2} and other relevant parameters are given in the main text. The two distinct paramagnetic regions surrounding the SDW order, labeled PM_1 and PM_2, represent the low- and high-moment regions, respectively.

is therefore not shown. Intraorbital SC and charge-density wave channels feature repulsive interactions, but intraorbital SC is induced from interorbital SC via SOC, though is small in comparison.

Taking into account interorbital SC and intraorbital SDW, the effective Hamiltonian is found as

$$\frac{H_{\text{eff}}}{N} = 2(U' - J_H)\sum_{a\neq b}\hat{\bar{\Delta}}^{\dagger}_{a/b}\cdot\hat{\bar{\Delta}}_{a/b} - 2U\sum_{a}\hat{\bar{m}}^{a}_{\mathbf{q}}\cdot\hat{\bar{m}}^{a}_{-\mathbf{q}} - J_H\sum_{a\neq b}\hat{\bar{m}}^{a}_{\mathbf{q}}\cdot\hat{\bar{m}}^{b}_{-\mathbf{q}}. \quad (1)$$

The orbital-singlet, spin-triplet, superconducting order parameter, $\hat{\Delta}^{l\dagger}_{a/b}$, is written as

$$\hat{\Delta}^{l\dagger}_{a/b} = \frac{1}{4N}\sum_{\mathbf{k}}[i\hat{\sigma}^{y}\hat{\sigma}^{l}]_{\sigma\sigma'}\left(c^{a\dagger}_{\mathbf{k},\sigma}c^{b\dagger}_{-\mathbf{k},\sigma'} - c^{b\dagger}_{\mathbf{k},\sigma}c^{a\dagger}_{-\mathbf{k},\sigma'}\right), \quad (2)$$

with $l = x, y, z$ and $a \neq b$ represents the sum over the unique pairs of orbital indices in (yz, xz, xy). The intraorbital SDW order parameter, $\hat{\bar{m}}^{a}_{\mathbf{q}}$, is given by

$$\hat{\bar{m}}^{a}_{\mathbf{q}} = \frac{1}{2N}\sum_{k} c^{a\dagger}_{\mathbf{k}+\mathbf{q}/2,\sigma}[\vec{\sigma}]_{\sigma,\sigma'}c^{a}_{\mathbf{k}-\mathbf{q}/2,\sigma'}, \quad (3)$$

where the electron operator $c^{a\dagger}_{\mathbf{k},\sigma}$ creates an electron in orbital a with spin σ.

To investigate the competition between SC and SDW order in these three systems, we must determine their tight-binding (TB) Hamiltonians. TB parameters are obtained from density functional theory (DFT) calculations, and listed in Tables I and II of Appendix A. The SC pairing itself is insensitive to the choice of TB parameters; however, the symmetry of the pairing state depends on the details as shown in Ref. [29]. While the pairing in the orbital basis has no momentum dependence, higher-angular momentum pairing can be revealed in the band basis due to momentum-dependent SOC or a combination of dispersion terms and SOC [28,29]. The A_{1g} pairing is favored by the atomic SOC considered here; however, all irreducible representations of the D_{4h} point group are possible from interorbital SC [37,38], with others favored by momentum-dependent SOCs [26,28,29]. This allows for gap nodes as well as a complex multicomponent order parameter as suggested by experiments [39,40], beyond the current study. Next, we explore the effects of orbital-dependent bilayer coupling on SC. We also examine hopping terms from staggered rotations, and show that this is responsible for the lack of SC in 327.

III. EVOLUTION OF SC

Self-consistent mean-field approximation (MFA) calculations are performed for the TB models of 214, $(327)_0$, and 327. $(327)_0$ uses the TB parameters from the single layer with interlayer hoppings added, referred to collectively as the bilayer coupling. In addition to bilayer coupling, intralayer hopping terms may be modified or added in 327 due to the staggered rotations of octahedra not present in the single layer.

The phase diagram for each of the three systems is shown in Fig. 1 as functions of the effective MFA interactions, $V_{\text{SDW}} \equiv U$ and $V_{\text{SC}} \equiv J_H - U'$. Comparing with 214, it is clear that the SC region is extended in $(327)_0$, while the SDW region is extended in 327. Since the precise values of U, U', and J_H are unknown, we set $U' = U - 2J_H$, and choose a set of (U, J_H) which gives SC in 214. These same values are used in 327 and $(327)_0$ since strong variation of local interactions is not expected across these systems. An asterisk in Fig. 5 corresponds to $(U, J_H) \sim (0.8, 0.4)$, where units of $2t^{xz}_{x} = 1$ in 214, given in Table I, are used throughout this work.

For the fixed values represented by the asterisk, the phase diagram in a magnetic field perpendicular to the layers is shown in Fig. 1, where areas of finite SC are shown in red. SC exists in 214 and is increased when bilayer coupling is added in $(327)_0$. The addition of staggered rotations in 327 destroys SC, which is replaced by a paramagnet. Further increasing the field eventually stabilizes SDW in 327, discussed below. This overall tendency is independent of the precise choice of (U, J_H) because the evolution of SC to SDW originates from the reduction SC and enhancement of SDW in 327.

To understand why SC is enhanced in $(327)_0$, consider the effect of the interlayer hopping in a two-orbital model. Interlayer hopping is orbital-dependent and largest for yz to yz and xz to xz hopping, while it is minimal between xy orbitals. A two-orbital model of xz (or yz) and xy gives insight into the effects of bilayer coupling. We use the basis $\Psi^{\dagger}_{k} = (\psi^{\dagger}_{k}, \mathcal{T}\psi^{T}_{k}\mathcal{T}^{-1})$, where $\mathcal{T}$ represents time reversal, and $\psi^{\dagger}_{k} = (c^{xz\dagger}_{k,1,\uparrow}, c^{xz\dagger}_{k,1,\downarrow}, c^{xy\dagger}_{k,1,\uparrow}, c^{xy\dagger}_{k,1,\downarrow}, c^{xz\dagger}_{k,2,\uparrow}, c^{xz\dagger}_{k,2,\downarrow}, c^{xy\dagger}_{k,2,\uparrow}, c^{xy\dagger}_{k,2,\downarrow})$, where the top and bottom layers are represented by the subscript 1 and 2, respectively. The kinetic and SOC parts of the Hamiltonian are then given by

$$H_k = \xi^{+}_{k}\rho_3\eta_0\tau_0\sigma_0 + \xi^{-}_{k}\rho_3\eta_0\tau_3\sigma_0 + \lambda\rho_3\eta_0\tau_2\sigma_1 + \tfrac{1}{2}t_{\perp}\rho_3\eta_1(\tau_0 + \tau_3)\sigma_0, \quad (4)$$

where η, τ, σ, and ρ are Pauli matrices representing the layer, orbital, spin, and particle-hole bases, respectively. The orbital dispersions in xz and xy are represented by $\xi^{xz/xy}_{k} = \xi^{+}_{k} \pm \xi^{-}_{k}$ and left in this general form here. Details of these dispersions used in the full three-orbital model are found in Appendix A.

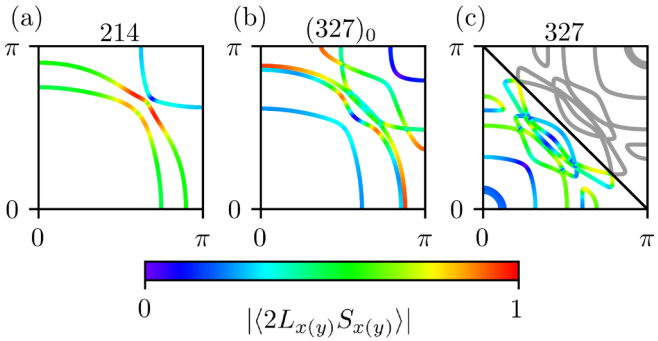

FIG. 2. Character of the mixing of orbitals and spins at the Fermi level at zero field, measured by $\langle 2L_{x(y)}S_{x(y)}\rangle$, for TB models of (a) 214, (b) the bilayer with no rotations, $(327)_0$, and (c) 327. Larger mixing favors interorbital SC [22]. The areas where these states mix most are shown in red, where pairing will be strongest. Introducing bilayer coupling that increases the band degeneracy leads to more areas where SC can form, as shown for $(327)_0$. This is not the case when staggered rotations are included in 327 consistent with self-consistent MFA results shown in Fig. 1.

The SOC is given by λ, and the interlayer hopping, $t_\perp$, exists only in xz.

The interorbital-singlet spin-triplet pairing, $\Delta_x^{xz/xy}$, with a d vector in the x direction, is written as

$$H_{\rm SC} = \Delta_x^{xz/xy}\rho_1\eta_0\tau_2\sigma_1. \tag{5}$$

Transforming $H_{\rm SC}$ to the band basis, i.e., the basis in which H_k is diagonal, it is clear how intraband pairing forms, and how the various terms affect the gap size; the magnitude of the intraband gaps in the two bands is

$$|\Delta^{\pm}_{\rm band}| = \frac{2\lambda\Delta_x^{xz/xy}}{\sqrt{\left(\xi_k^- \pm \frac{1}{2}t_\perp\right)^2 + 4\lambda^2}}. \tag{6}$$

This shows first that SOC is responsible for the formation of the intraband gap, consistent with previous works when $t_\perp = 0$ [28,29]. Second, it relates the interorbital SC pairing, $\Delta_x^{xz/xy}$, to the pairing on the band, $\Delta_{\rm band}$, where the pairing on the band is affected by the band dispersion $\sqrt{(\xi_k^- + \frac{1}{2}t_\perp)^2 + 4\lambda^2}$ or $\sqrt{(\xi_k^- - \frac{1}{2}t_\perp)^2 + 4\lambda^2}$. The pairing on one of the bands is increased by $t_\perp$ if the degeneracy of the bands is increased. Therefore, when the bilayer coupling brings two bands closer together near the Fermi level, the resulting bands feature a more significant mixture of the two orbitals with appropriate spin character via SOC, and thus are more ideal for interorbital SC to form.

The effect of the bilayer coupling on the orbital and spin mixing, shown for 214 in Figs. 2(a) and 2(b), is another way to understand the effect on interorbital SC pairing. This displays the trend of orbital and spin mixing via SOC, measured by $\langle 2L_xS_x\rangle$ or $\langle 2L_yS_y\rangle$, favorable for $\Delta_x^{xz/xy}$ or $\Delta_y^{yz/xy}$, within each of the bands at the Fermi level. Red areas are the most mixed, ideal for SC. Note that not all bands exhibit the increase in such mixing due to the bilayer; i.e., the bilayer can in principle decrease the band degeneracy, which works against the SC. For the 214 TB model though, we found that it works in favor of SC.

Next, we consider the effect of the staggered rotations present in 327. While the bilayer coupling may bring band energies closer together and increase degeneracy, orbital hybridization is detrimental to the formation of interorbital-singlet spin-triplet SC [28,33]. The hybridization from staggered rotations in 327 is included in Fig. 2(c), showing that areas of maximum mixing in the single layer and ideal bilayer have disappeared, destroying SC. This is consistent with the phase diagram of 327 in Fig. 1, obtained by self-consistent MFA calculations.

IV. SPIN-DENSITY WAVE ORDERING

In addition to interorbital SC, the Kanamori Hamiltonian also provides the intraorbital SDW instability. Specifically, with the Hubbard interaction, SDW order appears when an appropriate nesting vector exists. Previous studies on the magnetic susceptibility of 214 have found strong intraband nesting for $\mathbf{q} \approx (\pm\frac{\pi}{2}, \pm\pi)$ to $(\pm\frac{2\pi}{3}, \pm\pi)$ depending on TB parameters [25,41]. However, no SDW order is found in unstrained 214 at low temperatures, suggesting that this nesting is not sufficient for SDW order. Similar nesting is present in 327, with $\mathbf{q} \approx (\pm\frac{\pi}{2}, 0)$ to $(\pm\frac{\pi}{3}, 0)$ due to the unit cell doubling. In addition, there also exists the same vector rotated by $\frac{\pi}{2}$ (i.e., along the y direction instead). As in the case of 214, this nesting alone is not sufficient, as no SDW order forms at zero field. It was shown that SDW order is suppressed by SOC in 327 by reducing nesting [42], but the importance of SOC in this material has been recognized in explaining the dependence of the metamagnetic transition on the orientation of the field [42]. Additionally, experiments show a strong dependence of the formation of SDW order on the orientation of the field [16].

Although the nesting in 327 at zero field is not enough for SDW order to form, the presence of a van Hove singularity (vHS) was experimentally identified in the bilayer in the presence of a field [43], and it was suggested that the metamagnetic and nematic transitions are driven by the vHS [44–49]. We therefore consider the effect of nesting and vHSs together on the formation of SDW order in 327. Analysis of the 327 TB model obtained via DFT reveals a peak in the DOS just below the Fermi level. Introducing a magnetic field splits the peak in two, leading to a significant change in the magnetization once one peak reaches the Fermi level. The Fermi surface under a field, shown in the inset of Fig. 3(a), shows the additional bands crossing the Fermi level near $(\pm\pi, 0)$ and $(0, \pm\pi)$.

Considering possible ordering wave vectors, the intraorbital, intralayer transverse susceptibility is shown in Fig. 3(a). Importantly, the peak in the susceptibility increases when a field is present due to the additional bands crossing the Fermi level. This ordering wave vector corresponds to $\mathbf{q} \approx (0.3\pi, 0)$ in the reduced Brillouin zone, but slightly shifts as the field is changed. Details of the susceptibility calculations are found in Appendix B. To obtain numerical values, we perform self-consistent MFA calculations using Eq. (1) under a magnetic field. The region of SDW order is shown in blue in Fig. 1 where, for the choice of interaction and TB parameters, $B_{c1} \approx 2.3 \times 10^{-3}$ and $B_{c2} \approx 6.4 \times 10^{-3}$ with μ_B set to 1. Setting

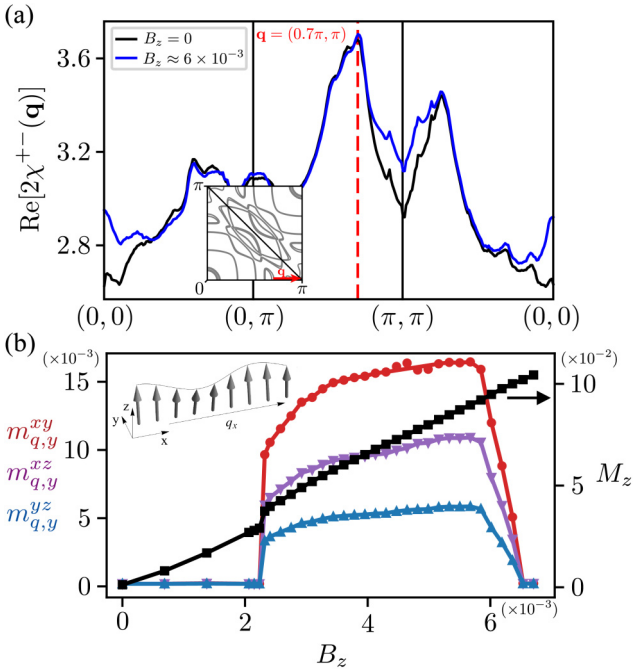

FIG. 3. (a) Transverse susceptibility calculations plotted over the extended Brillouin zone with and without a field. The peak at $\mathbf{q} = (0.7\pi, \pi)$ increases when the field is present and additional bands cross the Fermi level. The Fermi surface in the presence of a field (inset) shows the ordering wave vector of the reduced BZ. (b) Magnitude of the SDW order parameters, $m^a_{q,y}$, where a and y represent the orbital and magnetic moment direction, respectively, and M_z, the magnitude of the z magnetization. The inset shows a pictorial representation of the spins in the SDW state, with an overall magnetization in the z direction from the field, and an oscillating y component for $\mathbf{q}$ in the x direction.

t^x_{xz} to the DFT obtained value, B_{c1} is of order 10 T. However, these values are sensitive to the location of the vHSs in energy and the values of hopping parameters which can be further reduced by correlation effects beyond the MFA. Thus the precise field values require further study beyond the scope of the current work.

The SDW order parameters and magnetization are shown in Fig. 3(b), where the spin component is in the y direction in each of the three orbitals when the wave vector is in the x direction. The primary contribution comes from the xy orbital, and the secondary contribution from the xz orbital. The overall magnetization is in the z direction with the metamagnetic transition occurring at B_{c1}. A similar result is obtained when calculations are instead performed using a wave vector in the y direction; the SDW order occurs with spin in the x direction, with significant contributions from the xy then yz orbitals. Within this model of the bilayer, no SC regions are found.

V. DISCUSSION AND SUMMARY

The absence of SC in 327 must be considered when explaining SC in 214 due to the similarity of the two materials. The most significant differences, bilayer coupling and staggered rotations, primarily affect interorbital SC and therefore provide a natural explanation for the lack of SC in 327. The presence of SDW order in 327 under a field is another piece of the ruthenate puzzle. The Kanamori Hamiltonian provides a consistent framework for both SC and SDW order. The Hund's coupling plays an important role in stabilizing interorbital SC, while the Hubbard repulsion and Hund's coupling together lead to SDW order. These interactions plus the increase in the DOS occurring in a field, experimentally observed as a metamagnetic transition, allow SDW ordering to form. The interactions presented here are limited to on-site, but further neighbor interactions have been considered in interorbital SC studies of 214 [50]. Their effect on SDW order remains to be studied.

Some limitations of our theory arise from the finite size of the TB model and MFA. Experiments detect multiple metamagnetic transitions and two SDW phases with different ordering wave vectors all separated by less than 1 T [51]. Electron correlations beyond the MFA were shown to be important in the formation of the heavy bands [52], important for reproducing the narrow range over which the metamagnetic transitions and SDW phases occur. The interorbital SC presented here requires $U' < J_H$ within the MFA. It was shown by DMFT and other studies that such a requirement is not necessary beyond the MFA [23–25,53,54]. To corroborate the earlier numerical studies, we calculated pairing correlators via exact diagonalization on a small cluster and found interorbital pairing tendency occurring when J_H is about 20% of U. This tendency is related to the changes of charge configurations via Hund's coupling, shown in Appendix D.

An area of recent development requiring consideration going forward is possible SDW order in strained 214 [55]. While no experimental observations have been reported about the ordering wave vector or spin direction, this appears similar to 327 since SDW order occurs near a vHS. The shift of the vHS, however, is induced by strain, so while the q_x and q_y ordered states are degenerate in the bilayer, only one of these is chosen by the uniaxial strain. Further work is required to fully differentiate the two cases. Other recent experiments have studied surface layers of 214 [56], and the trilayer, $Sr_4Ru_3O_{10}$ [57], both of which feature staggered rotations. No SC is found in either, consistent with the current theory. However, future works are needed to estimate surface effects including broken inversion symmetry.

In summary, we showed that interorbital SC provides a natural explanation for both the presence of SC in 214 and lack of SC in 327. In 327, SC is destroyed by orbital hybridization introduced by staggered rotations, not present in 214. This same model finds intraorbital SDW ordering in 327 when the vHS reaches the Fermi level via a magnetic field. We believe that the lack of SC in 327 is an important piece of the puzzle to understand SC in 214, and therefore interorbital SC should remain among the promising candidates. Additionally, we predict that ideal $(327)_0$ can feature increased orbital degeneracy by tuning the bilayer coupling strength, and therefore can also exhibit interorbital SC with a possibly higher transition temperature.

TABLE I. Tight-binding parameters obtained for the single bilayer, 214, plus the additional bilayer coupling terms used to model the ideal bilayer, $(327)_0$, shown in parentheses. Note that the single layer and the ideal bilayer do not feature staggered rotations of the octahedra, so the staggered hopping terms are all 0 for both. Values that were not able to be obtained from DFT results are marked with an "x". While these values are important when considering the vHS in the real bilayer, they are not expected to have any significant effect in the single layer since flat bands near the Fermi level are not present. All values are shown in units of meV. Values listed in the main text are all given in units of $2t_x^{xz} = 1$.

t_x^{xz}	t_y^{xz}	$t_{x,y}^{xz}$	t_{2x}^{xz}	$t_{2x,y}^{xz}$
290.8	44.8	−16.8	−47.0	−13.5
t_{3x}^{xz}	t_{1D}	μ_{1D}	$t_{\perp}^{1D}$	$t_{\perp,x}^{xz}$
−3.2	10.1	295.9	(290.8)	(120.3)
t_x^{xy}	$t_{x,y}^{xy}$	t_{2x}^{xy}	$t_{2x,y}^{xy}$	$t_{2x,2y}^{xy}$
369.6	120.3	−4.2	20.3	14.1
t_{3x}^{xy}	$t_{3x,y}^{xy}$	$t_{3x,2y}^{xy}$	t_{4x}^{xy}	$t_{3x,3y}^{xy}$
4.8	4.4	5.5	1.9	4.0
$t_{4x,y}^{xy}$	$t_{4x,2y}^{xy}$	$t_{4x,3y}^{xy}$	t_{5x}^{xy}	$t_{5x,y}^{xy}$
2.6	3.1	2.9	x	x
μ_{xy}	$t_{\perp}^{xy}$	$t_{\perp,y}^{xz,xy}$	t^{stag}	$t_{\perp}^{\text{stag}}$
426.4	(44.8)	(10.1)	0	0

ACKNOWLEDGMENTS

We would like to thank P. Stavropoulos for useful discussion. This work was supported by the Natural Sciences and Engineering Research Council of Canada, Discovery Grant No. 06089-2016, and the Center for Quantum Materials at the University of Toronto. Computations were performed on the Niagara supercomputer at the SciNet HPC Consortium. SciNet is funded by the Canada Foundation for Innovation under the auspices of Compute Canada; the Government of Ontario; Ontario Research Fund - Research Excellence; and the University of Toronto.

APPENDIX A: TIGHT-BINDING MODEL

To obtain tight-binding parameters, we perform density functional theory calculations with the Vienna *ab initio* simulation package (VASP) [58], using the projector augmented-wave potential [59] and the Perdew-Burke-Ernzerhof exchange-correlation functional [60], with an energy cutoff of 400 eV. The relevant TB parameters are obtained using WANNIER90 [61], and are listed in Tables I and II.

The TB model is given by

$$\begin{aligned} H_k = & \sum_{k,a,l} \xi_k^a c_{k,l,\sigma}^{a\dagger} c_{k,l,\sigma}^{a} + \sum_{k,l} t_k c_{k,l,\sigma}^{xz\dagger} c_{k,l,\sigma}^{yz} + \text{H.c.} + \sum_k t_{\perp}^{1D} \left(c_{k,t,\sigma}^{yz\dagger} c_{k,b,\sigma}^{yz} + c_{k,t,\sigma}^{xz\dagger} c_{k,b,\sigma}^{xz} \right) + t_{\perp}^{xy} c_{k,t,\sigma}^{xy\dagger} c_{k,b,\sigma}^{xy} \\ & - 2t_{\perp,x}^{xz} \left(c_{k,t,\sigma}^{yz\dagger} c_{k,b,\sigma}^{yz} \cos k_y + c_{k,t,\sigma}^{xz\dagger} c_{k,b,\sigma}^{xz} \cos k_x \right) - 2t_{\perp,x}^{xz/xy} \left(\sin k_y \left[c_{k,b,\sigma}^{xy\dagger} c_{k,t,\sigma}^{xz} - c_{k,t,\sigma}^{xy\dagger} c_{k,b,\sigma}^{xz} \right] \right. \\ & \left. + \sin_x \left[c_{k,b,\sigma}^{xy\dagger} c_{k,t,\sigma}^{yz} - c_{k,t,\sigma}^{xy\dagger} c_{k,b,\sigma}^{yz} \right] \right) + \text{H.c.} \\ & + \sum_k 2t^{\text{stag}} (\cos k_x + \cos k_y) \left(c_{k,t,\sigma}^{yz\dagger} c_{k+Q,t,\sigma}^{xz} - c_{k,t,\sigma}^{xz\dagger} c_{k+Q,t,\sigma}^{yz} - c_{k,b,\sigma}^{yz\dagger} c_{k+Q,b,\sigma}^{xz} + c_{k,b,\sigma}^{xz\dagger} c_{k+Q,b,\sigma}^{yz} \right) + \text{H.c.} \\ & + \sum_k t_{\perp}^{\text{stag}} \left(c_{k,t,\sigma}^{yz\dagger} c_{k+Q,b,\sigma}^{xz} - c_{k,t,\sigma}^{xz\dagger} c_{k+Q,b,\sigma}^{yz} \right) + \text{H.c.}, \end{aligned} \tag{A1}$$

where $a \in (yz, xz, xy)$ represents the orbitals, and $l \in (t, b)$ is the layer index. The intraorbital dispersions are

$$\begin{aligned} \xi_k^{xz(yz)} = & -\mu_{1D} - 2t_x^{xz} \cos k_{x(y)} - 2t_y^{xz} \cos k_{y(x)} \\ & - 4t_{x,y}^{xz} \cos k_x \cos k_y - 2t_{2x}^{xz} \cos 2k_{x(y)} \\ & - 2t_{3x}^{xz} \cos 3k_{x(y)} - 4t_{2x,y}^{xz} \cos 2k_{x(y)} \cos k_{y(x)}, \end{aligned} \tag{A2}$$

$$\begin{aligned} \xi_k^{xy} = & -\mu_{xy} - \sum_n \left[2t_{nx}^{xy} (\cos nk_x + \cos nk_y) \right. \\ & \left. + 4t_{nx,ny}^{xy} \cos nk_x \cos nk_y \right] \\ & - \sum_{m \neq n} 4t_{mx,ny}^{xy} (\cos mk_x \cos nk_y + \cos nk_x \cos mk_y), \end{aligned} \tag{A3}$$

TABLE II. Tight-binding parameters obtained for the real bilayer, 327. All values are shown in units of meV. Note that the chemical potential listed here is slightly below a filling of 2/3 to ensure that the vHS is close enough to the Fermi level to produce the metamagnetic transition at a field value near the experimentally observed 7.9 T. The chemical potential used corresponds to a filling fraction of approximately 0.657.

t_x^{xz}	t_y^{xz}	$t_{x,y}^{xz}$	t_{2x}^{xz}	$t_{2x,y}^{xz}$
270.2	12.1	−15.1	−29.8	−10.1
t_{3x}^{xz}	t_{1D}	μ_{1D}	$t_{\perp}^{1D}$	$t_{\perp,x}^{xz}$
−3.5	12.6	282.9	281.6	90.6
t_x^{xy}	$t_{x,y}^{xy}$	t_{2x}^{xy}	$t_{2x,y}^{xy}$	$t_{2x,2y}^{xy}$
294.3	137.2	32.5	13.6	22.1
t_{3x}^{xy}	$t_{3x,y}^{xy}$	$t_{3x,2y}^{xy}$	t_{4x}^{xy}	$t_{3x,3y}^{xy}$
−12.5	10.3	1.34	8.99	2.2
$t_{4x,y}^{xy}$	$t_{4x,2y}^{xy}$	$t_{4x,3y}^{xy}$	t_{5x}^{xy}	$t_{5x,y}^{xy}$
−1.9	1.1	1.3	−3.76	0.7
μ_{xy}	$t_{\perp}^{xy}$	$t_{\perp,y}^{xz,xy}$	t^{stag}	$t_{\perp}^{\mathrm{stag}}$
400.7	18.6	13.6	84.5	64.3

where m and n are the integers listed in Table II describing the intraorbital hopping within the xy orbitals between sites separated by $m\hat{x}+n\hat{y}$ as well as $n\hat{x}+m\hat{y}$ by symmetry. The dispersion of the xy orbital includes further neighbor hopping terms to model the flatness of the bands near $(\pm\pi,0)$ and $(0,\pm\pi)$ of the Brillouin zone in the real bilayer material. The orbital mixing is given by

$$t_k = -4t_{1D}\sin k_x \sin k_y. \tag{A4}$$

The interlayer hoppings, $t_{\perp}^{1D}$ and $t_{\perp}^{xy}$, represent hopping between layers within orbitals directly above or below each other, while $t_{\perp,x}^{xz}$ is hopping in the xz (yz) orbital between layers and one lattice site over in the x (y) direction, and $t_{\perp,y}^{xz/xy}$ hopping between layers, one lattice site over in the y (x) direction, between xy and xz (yz) orbitals. The staggered hopping, t^{stag}, allowed by the staggered rotation, represents the hopping between NN $1D$ orbitals within a layer and changes sign between layers due to the opposite sense of the octahedra rotations between the layers, while $t_{\perp}^{\mathrm{stag}}$ occurs between $1D$ orbitals directly above or below each other. Finally, the SOC Hamiltonian is

$$H_{\mathrm{SOC}} = i\lambda \sum_i \sum_{abl} \epsilon_{abl} c_{i\sigma}^{a\dagger} c_{i\sigma'}^{b} \hat{\sigma}_{\sigma\sigma'}^{l}, \tag{A5}$$

where the strength of the SOC used is set to $\lambda = 62.5\,\mathrm{meV}$ throughout this work.

In calculations which feature a magnetic field in the z direction, the additional term included in the Hamiltonian is

$$H_B = -B_z \sum_i \left(2S_i^z + L_i^z\right). \tag{A6}$$

The total z magnetization calculated in the presence of the field is given by

$$M_z = \sum_i \left\langle 2S_i^z + L_i^z \right\rangle. \tag{A7}$$

APPENDIX B: SUSCEPTIBILITY

Defining the components of the spin operator for orbital $\alpha = (yz, xz, xy)$ and layer $l = (t, b)$ as

$$S_{\alpha l}^{a}(\mathbf{q}) = \sum_{\mathbf{k},\sigma\sigma'} c_{\mathbf{k}\alpha l\sigma}^{\dagger} \frac{\sigma_{\sigma\sigma'}^{a}}{2} c_{\mathbf{k}+\mathbf{q}\alpha l\sigma'}, \tag{B1}$$

the total bare spin susceptibility is calculated by summing over the orbital and layer indices in the Fourier transform of the imaginary-time spin-spin correlation function,

$$\chi^{ab}(\mathbf{q}, i\omega_n) = \sum_{\alpha,\beta,l,m} [\chi^{ab}]_{\beta m}^{\alpha l}(\mathbf{q}, i\omega_n),$$

$$[\chi^{ab}]^{\alpha l_{\beta m}}(\mathbf{q}, i\omega_n) = \frac{1}{N}\int_0^{\beta} d\tau e^{i\omega_n \tau} \left\langle T_\tau S_{\alpha l}^{a}(\mathbf{q},\tau) S_{\beta m}^{b}(-\mathbf{q},0)\right\rangle, \tag{B2}$$

where $\beta = \frac{1}{k_B T}$, τ is imaginary time, and T_τ is the imaginary-time ordering operator. To evaluate this we use the transformation to the band basis given by $c_{\mathbf{k}n} = \sum_s u_{ns}(\mathbf{k}) d_{\mathbf{k}s}$, where $n = (\alpha, l, \sigma)$, s indexes the bands, and $u_{ns}(\mathbf{k})$ are the coefficients of the unitary transformation. Evaluating the correlation function in terms of the Green's functions in the band basis and subsequently the Matsubara sum via contour integration, with the analytic continuation $i\omega_n \to w + i\eta$, the components of the static susceptibility are given by

$$\begin{aligned}[\chi^{ab}]_{\beta m}^{\alpha l}(\mathbf{q},0) = -\frac{1}{4N} \sum_{\mathbf{k},s,s',\sigma_1,\sigma_2,\sigma_3,\sigma_4} & u_{\alpha l\sigma_1,s}^{*}(\mathbf{k}) \sigma_{\sigma_1\sigma_2}^{a} u_{\alpha l\sigma_2,s'} \\ & \times (\mathbf{k}+\mathbf{q}) u_{\beta m\sigma_3,s'}^{*}(\mathbf{k}+\mathbf{q}) \sigma_{\sigma_3\sigma_4}^{b} u_{\beta m\sigma_4,s}(\mathbf{k}) \\ & \times \frac{f\left(\xi_{\mathbf{k}}^{s}\right) - f\left(\xi_{\mathbf{k}+\mathbf{q}}^{s'}\right)}{\xi_{\mathbf{k}}^{s} - \xi_{\mathbf{k}+\mathbf{q}}^{s'} + i\eta}.\end{aligned} \tag{B3}$$

Figure 4 shows the intralayer contribution to the transverse susceptibility from each orbital, $\sum_l [\chi^{+-}]_{\alpha l}^{\alpha l}(\mathbf{q})$, the intralayer contribution summed over the orbital index,

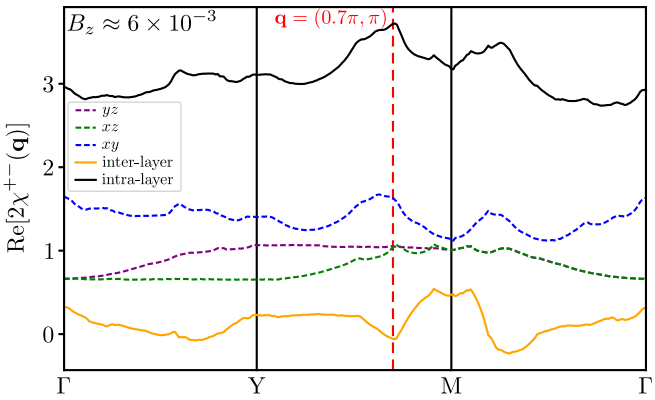

FIG. 4. Transverse susceptibility of the 327 model in the presence of a finite field. The intraorbital, intralayer susceptibilities are individually plotted, which provide the primary contributions to the ordering. The total intralayer susceptibility including intraorbital and interorbital contributions is also shown. Additionally, the total *inter*layer susceptibility is plotted, which, when included, may modify the ordering wave vector due to the differing locations of its peaks.

$\sum_{\alpha,\beta,l}[\chi^{+-}]^{\alpha l}_{\beta l}(\mathbf{q})$, and the interlayer contribution summed over the orbital index, $\sum_{\alpha,\beta,l\neq m}[\chi^{+-}]^{\alpha l}_{\beta m}(\mathbf{q})$.

APPENDIX C: FULL PHASE DIAGRAM

To show the behavior of all three models considered for various sets of interaction parameters, the full phase diagrams are shown in Fig. 5. The superconducting region expands when the bilayer coupling is added to the single-layer model; however, the superconducting region shrinks and the spin-density wave region is expanded when the staggered rotations are also added. The asterisks correspond to the values used in the main text, where superconductivity exists in 214 and $(327)_0$, while 327 remains a paramagnet at zero field and only exhibits SDW order when a field is introduced.

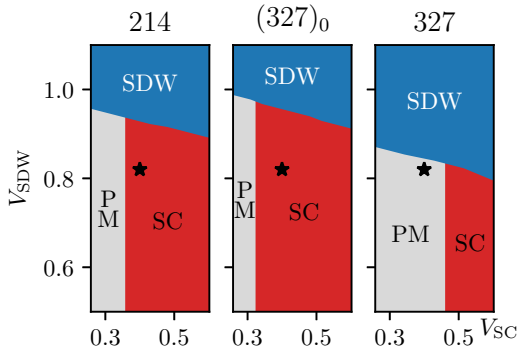

FIG. 5. Full phase diagram of Eq. (1) from the main text for each of the TB sets in Tables I and II, where $V_{\mathrm{SDW}} = U$ and $V_{\mathrm{SC}} = 3J_H - U$. All calculations are performed without a field. In the presence of a field, the SDW region of the 327 model expands due to the vHSs crossing the Fermi level. The asterisks correspond to the values used in the calculations presented in the main text.

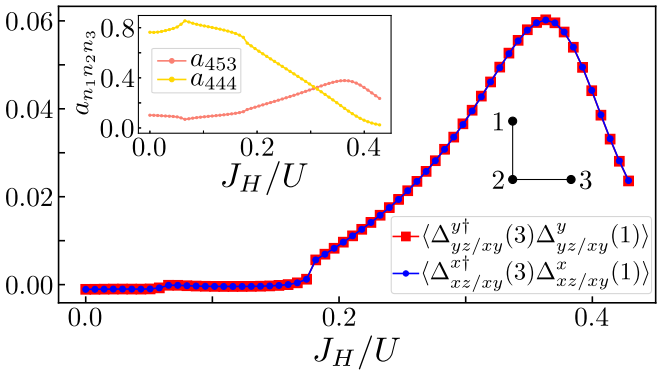

FIG. 6. Pairing correlators from three-site exact diagonalization calculations as a function of J_H/U, calculated for the 214 tight-binding parameters shown in Table I, and the Kanamori Hamiltonian using $U = 3.5$. The correlators are finite before the MFA-required minimum ratio of $J_H/U > 1/3$, suggesting that electron fluctuations can reduce the required Hund's coupling necessary for SC to form. The electron configurations are shown in the upper left inset, where $a_{n_1n_2n_3}$ refers to the weight of $d_1^{n_1}d_2^{n_2}d_3^{n_3}$ configuration in the wave function, where n_i represents the number of electrons at site i. The pairing correlators become finite at the interaction ratio corresponding to the sudden drop of the weight of the $d_1^4d_2^4d_3^4$ configuration and increase in the $d_1^4d_2^5d_3^3$ configuration, boosted by Hund's coupling. The a_{444} and a_{453} weights are shown, but other configurations also contribute to the wave function. The geometry of the three-site configuration is shown under the curve.

APPENDIX D: EXACT DIAGONALIZATION CORRELATORS

To extend the consideration of SC beyond the MFA, in Fig. 6, we show an exact diagonalization calculation for a three-site cluster as shown by the dots below the curve in the figure, containing three t_{2g} orbitals per site and 12 total electrons. Including spin the dimension of the Hilbert space is $\binom{18}{12} = 18\,564$. The Hamiltonian includes the same Kanamori interaction terms considered in the main text and the ground state is obtained with the Lanczos algorithm with a convergence tolerance of 10^{-15}. The pairing correlation function, $\langle\Delta^{l\dagger}_{a/b}(i)\Delta^{l}_{a/b}(j)\rangle$, for the interorbital-singlet spin-triplet pairings considered in the main text is evaluated between the two next-nearest-neighbor sites separated along the diagonal ($i = 3$, $j = 1$) as a function of J_H/U with the hopping parameters for 214 shown in Table I and $U = 3.5$. The pairing correlations for the $\Delta^{x}_{xz/xy}$ and $\Delta^{y}_{yz/xy}$ operators start to increase at $J_H/U \approx 0.18$, and are matched by an increase in charge fluctuations away from the $d_1^4d_2^4d_3^4$ configuration to configurations such as $d_1^4d_2^5d_3^3$, where d_i^n refers to n electrons at site i. The weight of the $d_1^4d_2^4d_3^4$ and $d_1^4d_2^5d_3^3$ configurations in the ground state wave function are shown in the upper left inset of Fig. 6, denoted a_{444} and a_{453}, respectively. Other configurations also contribute to the ground state wave function, but are omitted here. The inclusion of electron fluctuations as allowed by these calculations shows that the strict requirement of $J_H/U > 1/3$ is only necessary in the MFA where the effects of charge configurations such as $d_1^4d_2^5d_3^3$ combined with Hund's coupling cannot be taken into account.

[1] Y. Maeno, H. Hashimoto, K. Yoshida, S. Nishizaki, T. Fujita, J. G. Bednorz, and F. Lichtenberg, Superconductivity in a layered perovskite without copper, Nature (London) **372**, 532 (1994).

[2] A. P. Mackenzie and Y. Maeno, The superconductivity of Sr_2RuO_4 and the physics of spin-triplet pairing, Rev. Mod. Phys. **75**, 657 (2003).

[3] C. Kallin, Chiral p-wave order in Sr_2RuO_4, Rep. Prog. Phys. **75**, 042501 (2012).

[4] A. P. Mackenzie, T. Scaffidi, C. W. Hicks, and Y. Maeno, Even odder after twenty-three years: The superconducting order parameter puzzle of Sr_2RuO_4, npj Quantum Mater. **2**, 40 (2017).

[5] S. A. Kivelson, A. C. Yuan, B. Ramshaw, and R. Thomale, A proposal for reconciling diverse experiments on the superconducting state in Sr_2RuO_4, npj Quantum Mater. **5**, 43 (2020).

[6] R. S. Perry, L. M. Galvin, S. A. Grigera, L. Capogna, A. J. Schofield, A. P. Mackenzie, M. Chiao, S. R. Julian, S. I. Ikeda, S. Nakatsuji, Y. Maeno, and C. Pfleiderer, Metamagnetism and Critical Fluctuations in High Quality Single Crystals of the Bilayer Ruthenate $Sr_3Ru_2O_7$, Phys. Rev. Lett. **86**, 2661 (2001).

[7] S. A. Grigera, R. S. Perry, A. J. Schofield, M. Chiao, S. R. Julian, G. G. Lonzarich, S. I. Ikeda, Y. Maeno, A. J. Millis, and A. P. Mackenzie, Magnetic field-tuned quantum criticality in the metallic ruthenate $Sr_3Ru_2O_7$, Science **294**, 329 (2001).

[8] R. S. Perry, K. Kitagawa, S. A. Grigera, R. A. Borzi, A. P. Mackenzie, K. Ishida, and Y. Maeno, Multiple First-Order Metamagnetic Transitions and Quantum Oscillations in Ultrapure $Sr_3Ru_2O_7$, Phys. Rev. Lett. **92**, 166602 (2004).

[9] S. A. Grigera, P. Gegenwart, R. A. Borzi, F. Weickert, A. J. Schofield, R. S. Perry, T. Tayama, T. Sakakibara, Y. Maeno, A. G. Green, and A. P. Mackenzie, Disorder-sensitive phase formation linked to metamagnetic quantum criticality, Science **306**, 1154 (2004).

[10] K. Kitagawa, K. Ishida, R. S. Perry, T. Tayama, T. Sakakibara, and Y. Maeno, Metamagnetic Quantum Criticality Revealed by ^{17}O-NMR in the Itinerant Metamagnet $Sr_3Ru_2O_7$, Phys. Rev. Lett. **95**, 127001 (2005).

[11] R. A. Borzi, S. A. Grigera, J. Farrell, R. S. Perry, S. J. S. Lister, S. L. Lee, D. A. Tennant, Y. Maeno, and A. P. Mackenzie, Formation of a nematic fluid at high fields in $Sr_3Ru_2O_7$, Science **315**, 214 (2007).

[12] A. Mackenzie, J. Bruin, R. Borzi, A. Rost, and S. Grigera, Quantum criticality and the formation of a putative electronic liquid crystal in $Sr_3Ru_2O_7$, Physica C (Amsterdam) **481**, 207 (2012).

[13] J. A. N. Bruin, H. Sakai, R. S. Perry, and A. P. Mackenzie, Similarity of scattering rates in metals showing T-linear resistivity, Science **339**, 804 (2013).

[14] A. M. Berridge, A. G. Green, S. A. Grigera, and B. D. Simons, Inhomogeneous Magnetic Phases: A Fulde-Ferrell-Larkin-Ovchinnikov-Like Phase in $Sr_3Ru_2O_7$, Phys. Rev. Lett. **102**, 136404 (2009).

[15] A. M. Berridge, S. A. Grigera, B. D. Simons, and A. G. Green, Magnetic analog of the Fulde-Ferrell-Larkin-Ovchinnikov phase in $Sr_3Ru_2O_7$, Phys. Rev. B **81**, 054429 (2010).

[16] C. Lester, S. Ramos, R. S. Perry, T. P. Croft, R. I. Bewley, T. Guidi, P. Manuel, D. D. Khalyavin, E. M. Forgan, and S. M. Hayden, Field-tunable spin-density-wave phases in $Sr_3Ru_2O_7$, Nat. Mater. **14**, 373 (2015).

[17] C. Lester, S. Ramos, R. S. Perry, T. P. Croft, M. Laver, R. I. Bewley, T. Guidi, A. Hiess, A. Wildes, E. M. Forgan, and S. M. Hayden, Magnetic-field-controlled spin fluctuations and quantum criticality in $Sr_3Ru_2O_7$, Nat. Commun. **12**, 5798 (2021).

[18] T. M. Rice and M. Sigrist, Sr_2RuO_4: An electronic analogue of ^{3}He?, J. Phys.: Condens. Matter **7**, L643 (1995).

[19] K. Ishida, H. Mukuda, Y. Kitaoka, K. Asayama, Z. Q. Mao, Y. Mori, and Y. Maeno, Spin-triplet superconductivity in Sr_2RuO_4 identified by ^{17}O Knight shift, Nature (London) **396**, 658 (1998).

[20] A. Pustogow, Y. Luo, A. Chronister, Y.-S. Su, D. A. Sokolov, F. Jerzembeck, A. P. Mackenzie, C. W. Hicks, N. Kikugawa, S. Raghu *et al.*, Constraints on the superconducting order parameter in Sr_2RuO_4 from oxygen-17 nuclear magnetic resonance, Nature (London) **574**, 72 (2019).

[21] A. Chronister, A. Pustogow, N. Kikugawa, D. A. Sokolov, F. Jerzembeck, C. W. Hicks, A. P. Mackenzie, E. D. Bauer, and S. E. Brown, Evidence for even parity unconventional superconductivity in Sr_2RuO_4, Proc. Natl. Acad. Sci. USA **118**, e2025313118 (2021).

[22] C. M. Puetter and H.-Y. Kee, Identifying spin-triplet pairing in spin-orbit coupled multi-band superconductors, Europhys. Lett. **98**, 27010 (2012).

[23] S. Hoshino and P. Werner, Superconductivity from Emerging Magnetic Moments, Phys. Rev. Lett. **115**, 247001 (2015).

[24] S. Hoshino and P. Werner, Electronic orders in multiorbital Hubbard models with lifted orbital degeneracy, Phys. Rev. B **93**, 155161 (2016).

[25] O. Gingras, R. Nourafkan, A.-M. S. Tremblay, and M. Côté, Superconducting Symmetries of Sr_2RuO_4 from First-Principles Electronic Structure, Phys. Rev. Lett. **123**, 217005 (2019).

[26] H. G. Suh, H. Menke, P. M. R. Brydon, C. Timm, A. Ramires, and D. F. Agterberg, Stabilizing even-parity chiral superconductivity in Sr_2RuO_4, Phys. Rev. Research **2**, 032023(R) (2020).

[27] A. W. Lindquist and H.-Y. Kee, Distinct reduction of Knight shift in superconducting state of Sr_2RuO_4 under uniaxial strain, Phys. Rev. Research **2**, 032055(R) (2020).

[28] J. Clepkens, A. W. Lindquist, and H.-Y. Kee, Shadowed triplet pairings in Hund's metals with spin-orbit coupling, Phys. Rev. Research **3**, 013001 (2021).

[29] J. Clepkens, A. W. Lindquist, X. Liu, and H.-Y. Kee, Higher angular momentum pairings in interorbital shadowed-triplet superconductors: Application to Sr_2RuO_4, Phys. Rev. B **104**, 104512 (2021).

[30] A. Klejnberg and J. Spalek, Hund's rule coupling as the microscopic origin of the spin-triplet pairing in a correlated and degenerate band system, J. Phys.: Condens. Matter **11**, 6553 (1999).

[31] X. Dai, Z. Fang, Y. Zhou, and F.-C. Zhang, Even Parity, Orbital Singlet, and Spin Triplet Pairing for Superconducting $LaFeAsO_{1-x}F_x$, Phys. Rev. Lett. **101**, 057008 (2008).

[32] C. N. Veenstra, Z.-H. Zhu, M. Raichle, B. M. Ludbrook, A. Nicolaou, B. Slomski, G. Landolt, S. Kittaka, Y. Maeno, J. H. Dil, I. S. Elfimov, M. W. Haverkort, and A. Damascelli, Spin-Orbital Entanglement and the Breakdown of Singlets and Triplets in Sr_2RuO_4 Revealed by Spin- and Angle-Resolved Photoemission Spectroscopy, Phys. Rev. Lett. **112**, 127002 (2014).

[33] A. Ramires and M. Sigrist, Identifying detrimental effects for multiorbital superconductivity: Application to Sr_2RuO_4, Phys. Rev. B **94**, 104501 (2016).

[34] O. Vafek and A. V. Chubukov, Hund Interaction, Spin-Orbit Coupling, and the Mechanism of Superconductivity in Strongly Hole-Doped Iron Pnictides, Phys. Rev. Lett. **118**, 087003 (2017).

[35] A. K. C. Cheung and D. F. Agterberg, Superconductivity in the presence of spin-orbit interactions stabilized by Hund coupling, Phys. Rev. B **99**, 024516 (2019).

[36] A. Ramires and M. Sigrist, Superconducting order parameter of Sr_2RuO_4: A microscopic perspective, Phys. Rev. B **100**, 104501 (2019).

[37] W. Huang, Y. Zhou, and H. Yao, Exotic Cooper pairing in multiorbital models of Sr_2RuO_4, Phys. Rev. B **100**, 134506 (2019).

[38] S.-O. Kaba and D. Sénéchal, Group-theoretical classification of superconducting states of strontium ruthenate, Phys. Rev. B **100**, 214507 (2019).

[39] S. Benhabib, C. Lupien, I. Paul, L. Berges, M. Dion, M. Nardone, A. Zitouni, Z. Q. Mao, Y. Maeno, A. Georges, L. Taillefer, and C. Proust, Ultrasound evidence for a two-component superconducting order parameter in Sr_2RuO_4, Nat. Phys. **17**, 194 (2021).

[40] S. Ghosh, A. Shekhter, F. Jerzembeck, N. Kikugawa, D. A. Sokolov, M. Brando, A. P. Mackenzie, C. W. Hicks, and B. J. Ramshaw, Thermodynamic evidence for a two-component superconducting order parameter in Sr_2RuO_4, Nat. Phys. **17**, 199 (2021).

[41] S. Cobo, F. Ahn, I. Eremin, and A. Akbari, Anisotropic spin fluctuations in Sr_2RuO_4: Role of spin-orbit coupling and induced strain, Phys. Rev. B **94**, 224507 (2016).

[42] S. Raghu, A. Paramekanti, E. A. Kim, R. A. Borzi, S. A. Grigera, A. P. Mackenzie, and S. A. Kivelson, Microscopic theory of the nematic phase in $Sr_3Ru_2O_7$, Phys. Rev. B **79**, 214402 (2009).

[43] A. Tamai, M. P. Allan, J. F. Mercure, W. Meevasana, R. Dunkel, D. H. Lu, R. S. Perry, A. P. Mackenzie, D. J. Singh, Z.-X. Shen, and F. Baumberger, Fermi Surface and van Hove Singularities in the Itinerant Metamagnet $Sr_3Ru_2O_7$, Phys. Rev. Lett. **101**, 026407 (2008).

[44] H.-Y. Kee and Y. B. Kim, Itinerant metamagnetism induced by electronic nematic order, Phys. Rev. B **71**, 184402 (2005).

[45] H. Yamase and A. A. Katanin, Van Hove singularity and spontaneous Fermi surface symmetry breaking in $Sr_3Ru_2O_7$, J. Phys. Soc. Jpn. **76**, 073706 (2007).

[46] W.-C. Lee and C. Wu, Theory of unconventional metamagnetic electron states in orbital band systems, Phys. Rev. B **80**, 104438 (2009).

[47] C. M. Puetter, J. G. Rau, and H.-Y. Kee, Microscopic route to nematicity in $Sr_3Ru_2O_7$, Phys. Rev. B **81**, 081105(R) (2010).

[48] D. V. Efremov, A. Shtyk, A. W. Rost, C. Chamon, A. P. Mackenzie, and J. J. Betouras, Multicritical Fermi Surface Topological Transitions, Phys. Rev. Lett. **123**, 207202 (2019).

[49] C. H. Mousatov, E. Berg, and S. A. Hartnoll, Theory of the strange metal $Sr_3Ru_2O_7$, Proc. Natl. Acad. Sci. USA **117**, 2852 (2020).

[50] A. T. Rømer, P. J. Hirschfeld, and B. M. Andersen, Superconducting state of Sr_2RuO_4 in the presence of longer-range Coulomb interactions, Phys. Rev. B **104**, 064507 (2021).

[51] Y. Tokiwa, M. Mchalwat, R. S. Perry, and P. Gegenwart, Multiple Metamagnetic Quantum Criticality in $Sr_3Ru_2O_7$, Phys. Rev. Lett. **116**, 226402 (2016).

[52] M. P. Allan, A. Tamai, E. Rozbicki, M. H. Fischer, J. Voss, P. D. C. King, W. Meevasana, S. Thirupathaiah, E. Rienks, J. Fink, D. A. Tennant, R. S. Perry, J. F. Mercure, M. A. Wang, J. Lee, C. J. Fennie, E.-A. Kim, M. J. Lawler, K. M. Shen, A. P. Mackenzie *et al.*, Formation of heavy d-electron quasiparticles in $Sr_3Ru_2O_7$, New J. Phys. **15**, 063029 (2013).

[53] O. Gingras, N. Allaglo, R. Nourafkan, M. Côté, and A.-M. S. Tremblay, Frequency-dependent inter-pseudospin solutions to superconducting strontium ruthenate, arXiv:2201.08917.

[54] O. Gingras, N. Allaglo, R. Nourafkan, M. Côté, and A.-M. S. Tremblay, Coexistence of even- and odd-frequency superconductivity in correlated multi-orbital systems with spin-orbit coupling, arXiv:2201.08918.

[55] V. Grinenko, S. Ghosh, R. Sarkar, J.-C. Orain, A. Nikitin, M. Elender, D. Das, Z. Guguchia, F. Brückner, M. E. Barber, J. Park, N. Kikugawa, D. A. Sokolov, J. S. Bobowski, T. Miyoshi, Y. Maeno, A. P. Mackenzie, H. Luetkens, C. W. Hicks, and H.-H. Klauss, Split superconducting and time-reversal symmetry-breaking transitions, and magnetic order in Sr_2RuO_4 under uniaxial stress, Nat. Phys. **17**, 748 (2021).

[56] C. A. Marques, L. C. Rhodes, R. Fittipaldi, V. Granata, C. M. Yim, R. Buzio, A. Gerbi, A. Vecchione, A. W. Rost, and P. Wahl, Magnetic-field tunable intertwined checkerboard charge order and nematicity in the surface layer of Sr_2RuO_4, Adv. Mater. **33**, 2100593 (2021).

[57] G. Gebreyesus, P. Ngabonziza, J. Nagura, N. Seriani, O. Akin-Ojo, and R. M. Martin, Electronic structure and magnetism of the triple-layered ruthenate $Sr_4Ru_3O_{10}$, Phys. Rev. B **105**, 165119 (2022).

[58] G. Kresse and J. Hafner, *Ab initio* molecular dynamics for liquid metals, Phys. Rev. B **47**, 558 (1993).

[59] P. E. Blöchl, Projector augmented-wave method, Phys. Rev. B **50**, 17953 (1994).

[60] J. P. Perdew, K. Burke, and M. Ernzerhof, Generalized Gradient Approximation Made Simple, Phys. Rev. Lett. **77**, 3865 (1996).

[61] A. A. Mostofi, J. R. Yates, G. Pizzi, Y.-S. Lee, I. Souza, D. Vanderbilt, and N. Marzari, An updated version of wannier90: A tool for obtaining maximally-localised Wannier functions, Comput. Phys. Commun. **185**, 2309 (2014).